Elucidation of anionic and cationic redox reactions in a prototype sodium layered oxide cathode

Chen Cheng,[1+] Siyuan Li,[2+] Tiefeng Liu,[2] Yingying Yan,[1] Manling Ding,[1] Yue Hu,[1] Jinpeng Wu,[3*] Jinghua Guo,[3,4*] and Liang Zhang[1*]

1. Institute of Functional Nano & Soft Materials (FUNSOM), Jiangsu Key Laboratory for Carbon-Based Functional Materials & Devices, Joint International Research Laboratory of Carbon-Based Functional Materials and Devices, Soochow University, 199 Ren'ai Road, Suzhou 215123, Jiangsu, China
2. College of Materials Science and Engineering, Zhejiang University of Technology, Hangzhou 310014, Zhejiang, China
3. Advanced Light Source, Advanced Light Source, Lawrence Berkeley National Laboratory, Berkeley, California 94720, USA
4. Department of Chemistry and Biochemistry, University of California, Santa Cruz, California 95064, USA

[+]These two authors contributed equally to this work.

*Email: jguo@lbl.gov (Jinghua Guo); liangzhang2019@suda.edu.cn (Liang Zhang); jinpeng@lbl.gov (Jinpeng Wu)

Abstract

The ever-increasing demand for large-scale energy storage has driven the prosperous investigation of sodium-ion batteries (NIBs). As a promising cathode candidate for NIBs, P2-type $Na_{2/3}Ni_{1/3}Mn_{2/3}O_2$ (NaNMO), a prototype sodium layered oxide, has attracted extensive attention because of its high operating voltage and high capacity density. Although its electrochemical properties have been extensively investigated, the fundamental charge compensation mechanism, i.e., the cationic and anionic redox reactions, is still elusive. In this report, we have systematically investigated the transition metal and oxygen redox reactions of NaNMO nanoflakes using bulk-sensitive soft X-ray absorption spectroscopy (sXAS) and full-range mapping of resonant inelastic X-ray scattering (mRIXS) from an atomic-level view. We show that the bulk Mn^{3+}/Mn^{4+} redox couple emerges from the first discharge process with the increment of inactive Mn^{3+} upon cycling, which may have a negative effect on the cyclability. In contrast, the bulk Ni redox mainly stems from the Ni^{2+}/Ni^{3+} redox couple, in contrast to the conventional wisdom of the Ni^{2+}/Ni^{4+} redox couple. The quantitative analysis provides unambiguous evidence for the continuous reduction of the average valence state of Mn and Ni over extended cycles, leading to the voltage fading. In addition, we reveal that the oxygen anions also participate in the charge compensation process mainly through irreversible oxygen release rather than reversible lattice oxygen redox. Such understanding is vital for the precise design and optimization of NaNMO electrodes for rechargeable NIBs with outstanding performance.

Keywords: sodium ion batteries, NaNMO nanoflakes, transition metal redox, oxygen redox, soft X-ray spectroscopy

Introduction

With increasing concerns about the environmental pollutions and resource shortages, it is desirable to develop new electrical energy storage systems with high energy density and low cost to alleviate this situation. Currently, lithium-ion batteries (LIBs) are one of the dominant energy storage devices, which have been successfully applied in our daily lives.[1-7] However, considering the geographically constrained lithium resources in the earth and the increased production costs, it is highly necessary to develop alternative energy storage systems utilizing earth-abundant elements.[8-9] Sodium is nature-abundant and cost-effective, which has similar chemical properties to lithium. As a consequence, sodium-ion batteries (NIBs) could be a promising alternative to LIBs for their potential applications in large-scale energy storage systems, which have attracted extensive attention recently.[10-11]

For NIBs, the cathode materials play a vital role for determining the overall performance, e.g., power density, energy density, and lifetime.[12-13] Several types of materials, such as sodium transition-metal layered oxides, pyrophosphate, NASICON-based compounds, and metal hexacyanoferrates, have been explored as the cathode materials for NIBs.[13-15] Among them, sodium transition-metal layered oxides Na_xTMO_2 (TM refers to transition metal) have attracted extensive attention mainly because of their advantages of facile synthesis, simple structures, and high capacities.[14, 16] Depending on the occupied Na sites and stacking sequence of O layers, Na_xTMO_2 can be generally categorized into P2 and O3 phases. In contrast to O3 counterparts, P2-type layered Na_xTMO_2 demonstrates a better structure stability during the sodiation/desodiation process due to its more open framework structure and prismatic paths within TMO_2 slabs, which enables it to be one of the most promising cathodes for NIBs with high specific capacity and low polarization.[17-19]

Specifically, the P2-type Mn-based Na_xMnO_2 materials are considered as excellent candidates for NIBs because of the environmental sustainability and low cost nature of Mn element.[20-22] However, the structure of P2-type Na_xMnO_2 is not stable mainly because of the high-spin Jahn-Teller active Mn^{3+} centers.[23] By introducing Ni ions into P2-type Na_xMnO_2 to increase the valence state of Mn ions to +4, the derived material, such as P2-type $Na_{2/3}Ni_{1/3}Mn_{2/3}O_2$ (NaNMO), displays a greatly improved structure stability and electrochemical performance.[24-32] For example, NaNMO delivers a high discharge capacity of ~160 mAh/g in the voltage range of 2.0-4.5 V with an average discharge voltage of ~3.7 V.[24, 33] However, the material undergoes a fast capacity fading over extended cycles, which may be attributed to the undesired P2-O2 phase transition in high-voltage regions.[20] This issue has been significantly mitigated by doping inactive elements into the transition-metal (TM) layers of NaNMO prototype, with the goal of eliminating phase transformations during cycling but at the expense of lower capacity.[18, 34-35]

In this manner, it is of profound significance to achieve high and stable discharge capacities for NaNMO cathode material. Consequently, fundamental understanding of the redox reaction and capacity fading mechanism of NaNMO is indispensable for tailoring the material to achieve an outstanding performance, which is still under active debate between different scenarios.[18, 25-30, 36-37] For example, a number of previous reports believed that all of the Na ions in NaNMO can be reversibly (de)intercalated based on the Ni^{2+}/Ni^{4+} redox couple,[18, 25, 33-34, 36] while the other reports claimed that not only transition metal cations but also oxygen anions are involved in the reversible redox processes over cycling.[27]

In this work, we have qualitatively and quantitatively investigated the TM and oxygen reactions of NaNMO prototype electrode materials by a combination of bulk-sensitive soft X-ray absorption spectroscopy (sXAS) and full-range mapping of resonant inelastic X-ray scattering (mRIXS), with a focus mainly on the TM (i.e., Mn and Ni) L-edge and O K-edge. The TM L-edge corresponds to the transitions from 2p to valence 3d states, which are more sensitive to the valence electron states and can be easily quantified.[38-40] This is in contrast to the more frequently utilized hard X-ray TM K-edge, which can only detect the edge shifting of the 1s-4p transition features.[41] It should be noted that the bulk-sensitive mode of sXAS, e.g., total fluorescence yield (TFY), suffers from the spectral distortion due to self-absorption effect,[42] especially for Mn element,[43] which may require further theoretical calculations for quantitative analysis. Here, we obtain the non-distorted bulk Mn L-edge inverse partial fluorescence yield (iPFY) through mRIXS to perform the straightforward quantitative analysis.[42] Moreover, the oxygen reaction activity of NaNMO is validated by mRIXS, which has been proven to be one of the most sensitive and reliable characterization techniques for detecting reversible oxygen redox upon cycling.[38, 44-45]

Results and discussion

Structure of NaNMO

The crystallographic structure of the as-prepared NaNMO nanoflakes was examined by X-ray diffraction (XRD) (Figure 1a). The XRD pattern shows the typical diffraction peaks of a hexagonal P2-type phase with space group P63/mmc. In this structure, Na^+ ions occupy two different trigonal prismatic sites, where Na_eO_6 and Na_fO_6 triangular prisms share edges and faces with MO6 (M = Ni and Mn) octahedral sites, respectively.[27,29] The SEM image of the NaNMO powder shown in Figure 1c exhibits micrometer-sized irregular particles due to the solid-state reaction process. The size of the NaNMO nanoflakes is in the range of 2-3 μm with a thickness of several ten to hundred nm. As the magnification increases, the NaNMO particles exhibit clean and smooth surfaces (Figure 1d), indicating that the material is well crystallized.

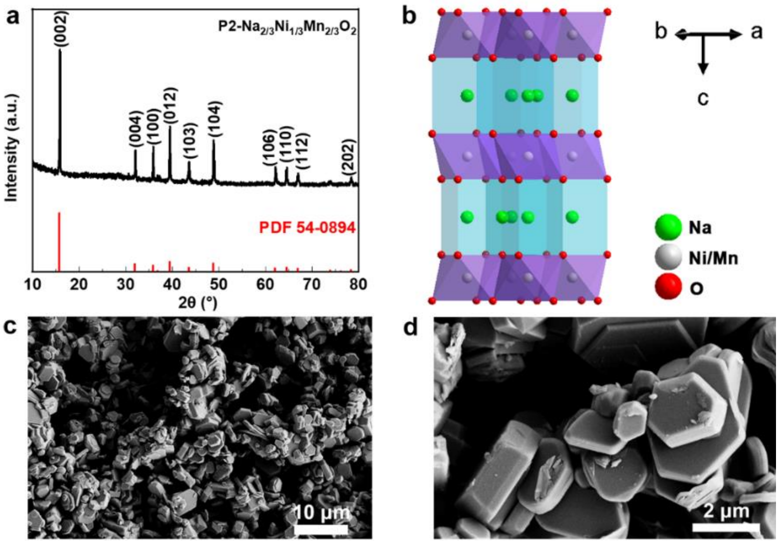

Figure 1. (a) XRD pattern of as-prepared NaNMO nanoflakes. (b) Schematic illustration of the crystal structure. (c,d) SEM images of as-prepared NaNMO nanoflakes.

Electrochemical performance of NaNMO electrode

The electrochemical performance of NaNMO electrode was evaluated through galvanostatic charge/discharge process between 2.0 and 4.5 V using 1M $NaClO_4$ in EC/PC (1/1 wt) as the electrolyte. As displayed in Figure 2, there are three voltage platforms for the first charge/discharge voltage profiles. The plateaus at the voltage below 4.0 V could correspond for single P2 phase intercalation, while the long plateau at 4.2 V may originate from P2 to O2 phase transition.[27, 29, 31, 36, 46] The NaNMO electrode delivers a first charge capacity of ca. 160 mAh g^{-1}, which is close to the complete extraction of 2/3 Na per formula unit.[27, 37] The subsequent discharge process demonstrates a reversible electrochemical behavior, corresponding to a specific capacity of 160 mAh g^{-1}. However, all the plateaus, especially for the plateaus above 4.0 V, decay rapidly with increasing the cycle number (Figure 2b and S1).

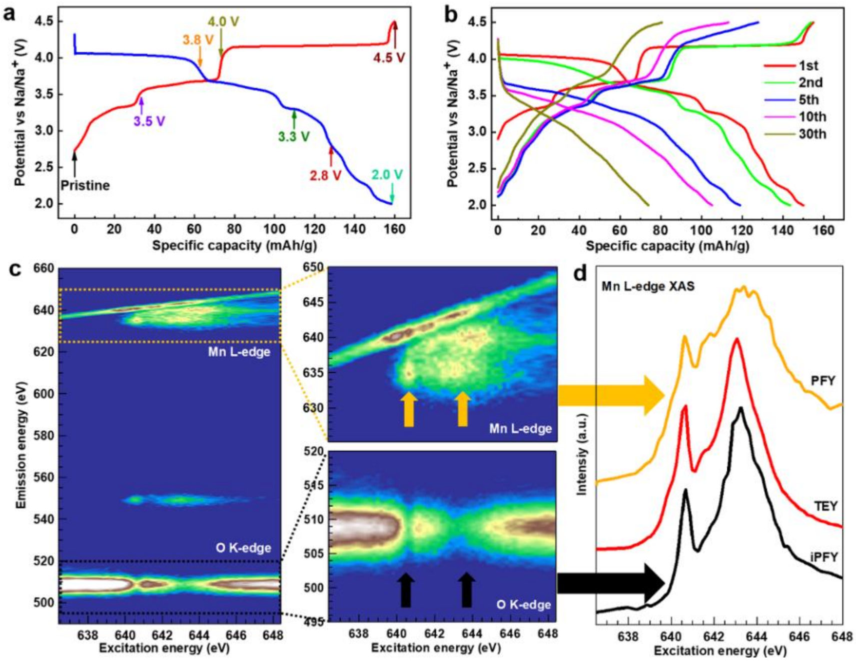

Figure 2. (a) The charge and discharge profiles of NaNMO at 0.1 C for the first cycle. The points measured by sXAS and RIXS are marked with arrows. (b) The voltage profiles of different cycles at 0.2 C. (c) The mRIXS images of pristine NaNMO with excitation energy at Mn L-edge range, but with emission energy at Mn L-edge and O K-edge. (d) The Mn L-edge sXAS spectra of pristine NaNMO measured in different modes.

In the following part, we will quantitatively elucidate the charge compensation mechanism of NaNMO upon Na extraction/insertion, by utilizing the soft X-ray spectroscopies, including both conventional sXAS and advanced mRIXS.[47]

Cationic redox behavior upon 1st cycle

Because of the severe self-absorption effect, the bulk-sensitive mode of Mn L-edge sXAS, i.e. TFY, suffers great distortion.[43] As shown in Figure 2c, under the excitation of Mn L-edge at 637-648 eV, there are not only Mn L-edge emission features, but also O K-edge emission features. The intensity of the non-resonant O K-edge emission is affected by the absorption coefficient of the incident X-ray at the corresponding Mn L-edge energy range, resulting in the appearance of dips at the same excitation energies of Mn L-edge absorption peaks (marked by arrows in Figure 2c). The Mn L-edge iPFY, which can be obtained by the inversed O K-edge PFY through integrating the mRIXS intensity within the O K-edge emission range (495-520 eV, Figure 2c), is a non-distorted and bulk-sensitive probe of the intrinsic Mn L-edge coefficient absorption.[38] We will utilize Mn L-edge iPFY for the following analysis on the bulk Mn state.

The Mn L-edge iPFY (Figure 2d) spectrum exhibits an exact Mn^{4+} spectrum for the pristine NaNMO, in contrast to the conventional sXAS results in TEY and PFY modes, which enables the quantitative fitting of the bulk Mn oxidation states. In the following paragraphs, we will mainly focus on the Mn L-edge iPFY results collected through full-range mRIXS and also their comparison with the surface-sensitive TEY results.

The quantitative analysis of the oxidation state of Mn as a function of state of charge (SOC) during the initial cycle is obtained by fitting the Mn L-edge iPFY using a linear combination of the distinct lineshape of $Mn^{2+/3+/4+}$ reference spectra shown at the bottom of Figure 3a. The fitting results (dotted lines) are in good agreement with the experimental results (solid lines), as shown in Figure 3a, providing a reliable determination of the Mn oxidation states in bulk. The values of Mn valence percentages from the fitting results are plotted in Figure 3c. The Mn^{4+} of pristine NaNMO remains unchanged until the voltage drops below 2.8 V during discharge, indicating that the Mn redox in the bulk is suppressed during the initial charge process. At fully discharged state (2.0 V), the electrode has about 25% Mn^{3+} and 6% Mn^{2+}, corresponding to 0.25 mol electron transfer per mol of NaNMO due to bulk Mn reduction. In contrast, the content of Mn^{2+} at the end of first discharge is much higher on the surface, as seen directly through the TEY spectra (Figure S2). The phenomenon may be related to the electrode-electrolyte surface reactions, which has been frequently observed for other Mn-containing oxide electrodes.[38, 43, 48]

Using the similar fitting method, we have also quantitatively analyzed the Ni L-edge TFY sXAS results (Figure 3b and 3d). Note that the self-absorption effect is negligible for Ni L-edge TFY spectra because of the large energy separation between O K-edge and Ni L-edge, in contrast to that of Mn L-edge TFY spectra mentioned. The content of Ni^{3+} is continuously increasing to 37% during the charge process with negligible amount of Ni^{4+}, while the content of Ni^{2+} is dropped to about 63%. During the following discharge process, the content of Ni^{2+} is almost fully recovered after discharge to 2.8 V, indicating the high reversibility of Ni^{2+}/Ni^{3+} redox reaction. The quantified electron transfer caused by bulk Ni redox reaction is 0.12 mol per NaNMO unit.

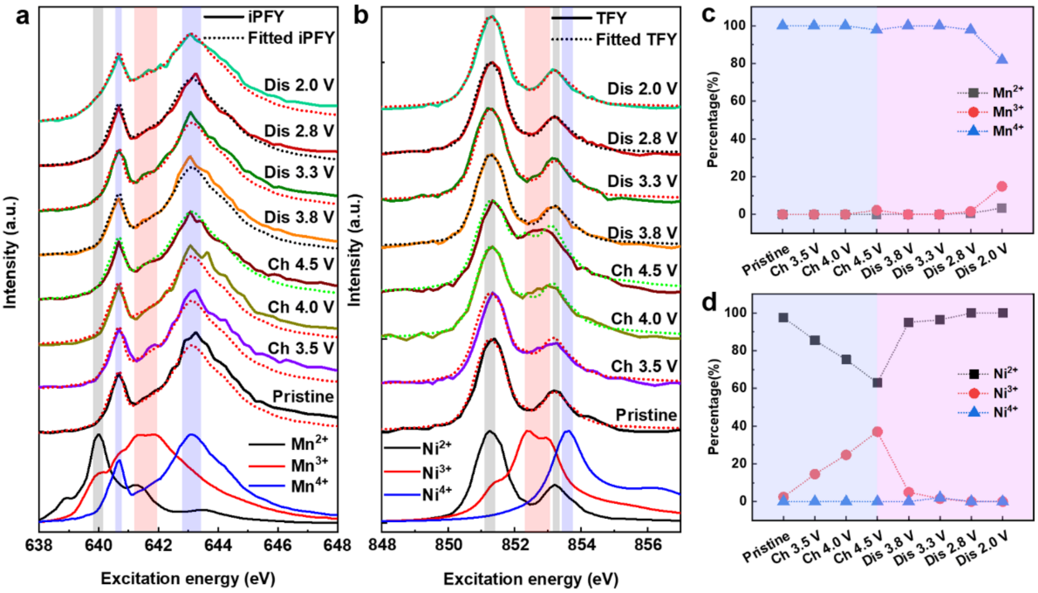

Figure 3. (a) Mn L-edge iPFY (solid line) and fitted iPFY (dashed line), (b) Ni L-edge TFY (solid line) and fitted TFY (dashed line) spectra of NaNMO at different electrochemical potentials as marked by the arrows in Figure 2a. The reference spectra are plotted at the bottom of each figure for comparison. (c,d) The fitting results of Mn and Ni valence distributions as a function of electrochemical potentials, respectively.

Several important conclusions can be achieved based on the Mn and Ni L-edge spectroscopic observation. Firstly, Ni^{2+}/Ni^{3+} is the redox couple in the voltage range of 2.8-4.5 V, in contrast to the conventional wisdom that the capacity of NaNMO mainly arises from the Ni^{2+}/Ni^{4+} redox reaction.[27, 30-31, 37] Actually, the Ni L-edge TFY sXAS spectrum of NaNMO charged to 4.5 V reported by Li et al. resembles the Ni^{3+} rather than Ni^{4+} reference spectrum, further supporting our assumption here. In addition, Guo et al. demonstrated that the Ni^{2+}/Ni^{3+} redox couple is responsible for the charge compensation mechanism of Ti-substituted NaNMO in the 2.5 V to 4.15 V voltage window.[18] Secondly, the Mn is also electrochemically active in the voltage range of 2.0-2.8 V with Mn^{3+}/Mn^{4+} as the main redox couple, although the surface has a high content of Mn^{2+} due to the surface reaction. Thirdly, the charge compensation of Mn and Ni redox is totally 0.12 mol during charging, and 0.37 mol (0.25 + 0.12 mol) during discharging, while the total charge compensation derived from the electrochemical experiment (Figure 2a) is ~0.61 mol for both charging and discharging. These results suggest that oxygen anions should also be involved in the charge compensation process, in addition to the presence of strong surface reactions discussed above.

Anionic redox upon the 1st cycling

To elucidate the charge compensation process of oxygen anions, we therefore measured O K-edge mRIXS for NaNMO electrodes at different SOC of the first cycle, as displayed in Figure 4. The mRIXS maps the fluorescence intensity as a function of absorption (y axis) and emission (x axis) energy, which can unambiguously resolve the lattice oxidized oxygen features that are buried in conventional sXAS.[38, 44-45, 49] The vertical stripes at excitation energies above 535 eV correspond to the O 2p-TM 4sp hybridization states, and the broad emission features at excitation energies below 532 eV (marked with circle) are attributed to the O 2p-TM 3d states.[49] More specifically, the large emission feature at an excitation energy of 529.5 eV is related to the t_{2g} state, while the relatively small emission feature at an excitation energy of 531.5 eV is attributed to the e_g state. Upon charging, the t_{2g} features get broadened in lineshape due to its more covalent nature with the increase of the TM oxidation states,[38, 44-45] consistent with many previous sXAS results but irrelevant to oxygen redox states.[27, 32, 50] This is also visualized in the PFY spectra by integrating the main O K-edge signal within the 519-529 eV emission energy, where the enhancement of the sXAS feature at ~529 eV is clearly observed after charging to 4.5 V (Figure 4d).

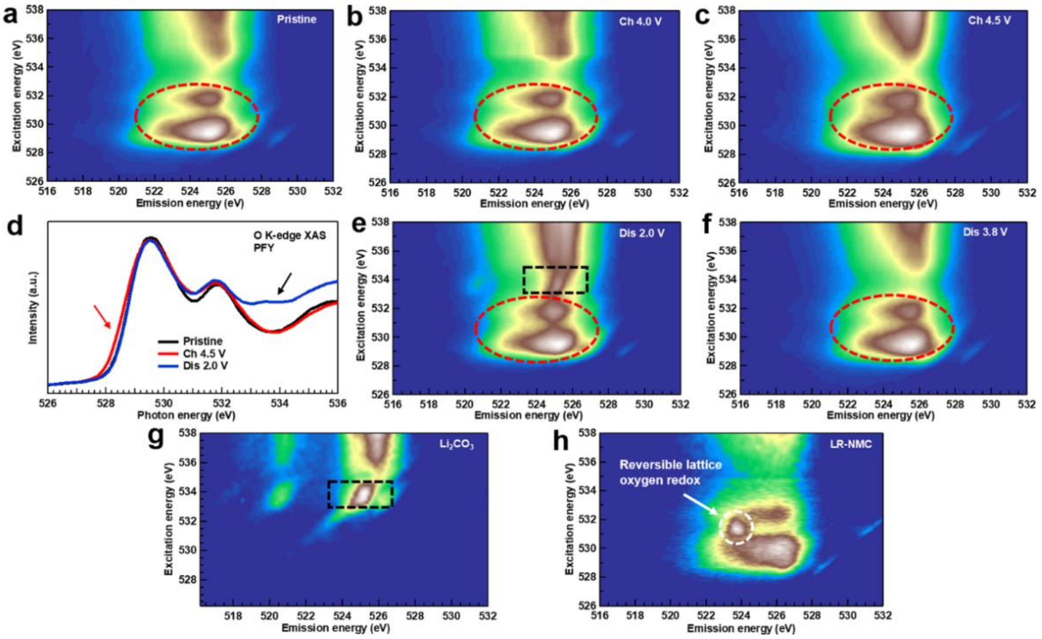

Figure 4. (a-f) The O K-edge mRIXS images of NaNMO at different SOC as marked in Figure 2a. The red cycles highlight the O 2p-TM 3d hybridization states. The PFY spectra extracted from mRIXS are shown in Figure 4d. The red and black arrows highlight the spectral shape change of t_{2g} state and CO_3^{2-}, respectively. (g) The mRIXS map of Li_2CO_3. (h) The mRIXS map of LR-NMC. The white arrow points to the characteristic reversible lattice oxygen redox feature, which is absent for NaNMO at different SOC.

However, the fingerprint feature of lattice oxidized oxygen, usually located at 531.0 eV excitation energy and 523.7 eV emission energy (Figure 4h, the mRIXS of lithium-rich NMC cathode charged to 4.5 V),[49] is absent during the whole discharge and charge processes, indicating no reversible lattice oxygen redox is involved in NaNMO. It is very likely that the oxygen is released from the lattice to form O_2 or to attack the electrolyte to form CO_2.[51] The release of oxygen could be caused by the unfavorable TM-O covalent bonding, which is not strong enough for stabilizing the oxidized oxygen species.[52] During the discharge process (Figure 4e and 4f), the t_{2g} feature tends to shrink due to the reduction of Ni and Mn, leading to the decrease of the pre-edge feature of O K-edge XAS (Figure 4d).

Interestingly, a specific mRIXS feature at 525 eV with an excitation energy of 533.8 eV (marked as black arrow and rectangle in Figure 4d and 4e, respectively) emerges after discharge to 2.0 V, which is also found in Li_2CO_3 reference (Figure 4g). Therefore, this O K-edge mRIXS feature can be used a reliable spectroscopic fingerprint of CO_3^{2-} in bulk. It should be mentioned that the formation of CO_3^{2-} concurrently occurs at the bulk and surface, because the CO_3^{2-} feature is observable in both bulk-sensitive TFY and surface-sensitive TEY O K-edge sXAS (Figure S3), with a more pronounced line shape change for the latter. The formation of CO_3^{2-} is most likely due to the decomposition of electrolyte, which can also contribute to the discharge capacity to some extent, as observed for other transition metal oxide electrodes before.[32, 53]

Evolution of TMs/O redox activities upon extended cycles

To further understand the capacity fading mechanism of NaNMO electrodes over extended cycles, we also measured the Mn L-edge iPFY (Figure 5a and 5c) and Ni L-edge TFY (Figure 5b and 5d) sXAS of NaNMO electrodes at fully charged (4.5 V) and discharged (2.0 V) sates after 2 and 30 cycles. The iPFY analysis of the Mn state indicates that Mn^{3+}/Mn^{4+} redox couple remain active upon cycling, but the amount of Mn^{3+} displays a remarkable increment from 1% for 2nd charge to 16% for 30th charge. The increment of the inactive Mn^{3+} aggravates the Jahn-Teller effect, which may have a negative effect on the cyclability.[38] Interestingly, the Mn^{2+} on the surface shows a much higher content as seen directly through the corresponding TEY spectra (Figure S2), This observation is related to the surface reduction reaction and oxygen release effect discussed above.

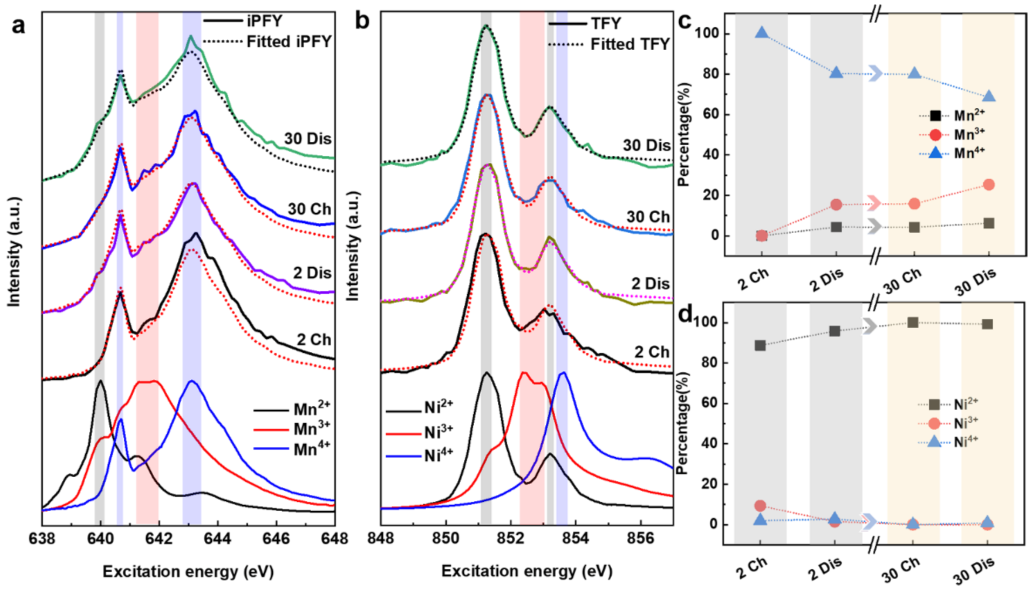

Figure 5. (a) Mn L-edge iPFY (solid line) and fitted iPFY (dashed line), (b) Ni L-edge TFY (solid line) and fitted TFY (dashed line) spectra of NaNMO at the charged and discharged states after the 2nd and 30th cycles. The reference spectra are plotted at the bottom of each figure for comparison. (c,d) The fitting results of Mn and Ni valence distributions as a function of electrochemical potentials, respectively.

In contrast, the reversibility of Ni^{2+}/Ni^{3+} redox couple gradually decreases and then totally vanishes after 30 cycles, as shown in Figure 5d, which is one main reason for the capacity fading of NaNMO over cycling. The deactivation of Ni^{2+}/Ni^{3+} redox couple may be related to the microstructural defects induced by the oxygen release,[54] which needs further detailed and comprehensive investigation to clarify. Another thing that should be noted is that the TM valence drop can result in the voltage fading for Li-rich cathode materials.[54] Our quantitative analysis of Mn and Ni L-edge sXAS directly proves the continuously reduced Mn and Ni valence upon cycling, which could lead to the voltage fading shown in Figure 2b.

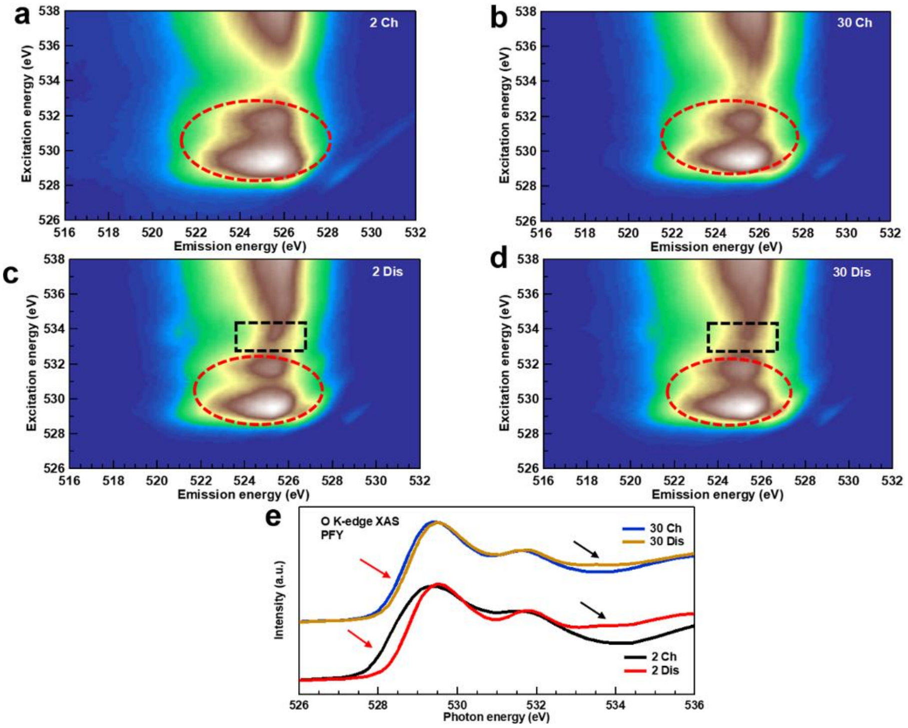

Figure 6. (a-d) The O K-edge mRIXS images of NaNMO at the charged and discharged states after the 2nd and 30th cycles. The red cycles highlight the O 2p-TM 3d hybridization states. (e) The corresponding PFY spectra extracted from mRIXS results. The red and black arrows highlight the spectral shape change of t_{2g} state and CO_3^{2-} upon cycling, respectively.

To decipher the oxygen activity upon extended cycling, we also recorded the O K-edge mRXIS of NaNMO after 2 and 30 cycles (Figure 6). Similar to the observation of the 1st cycle, the mRIXS results of NaNMO upon extended cycles (Figure 6a-d) do not show the characteristic features of lattice oxygen redox state, with only the enhancement during charge and depression during discharge of the t_{2g} state. The evolution of Mn and Ni valence upon cycling results in the change of the TM 3d-O 2p hybridization strength and thus the intensity of t_{2g} state (Figure 6e).

Note that due to the gradual degradation of Ni^{2+}/Ni^{3+} redox reaction, the intensity change of t_{2g} state is much weaker for the 30th cycle compared with that of the 2nd cycle. Because the Ni and Mn redox only contributes to part of the observed specific capacity of NaNMO, it is obvious that the oxygen anions also participate in the charge compensation process upon cycling, similar to the behavior of the first charge-discharge process. The mRIXS results unequivocally suggest that the charge compensation of oxygen anions is mainly in the manner of irreversible oxygen release rather than reversible lattice oxygen redox.[32]

It should be mentioned that the reversibility of oxygen redox of Na_xMnO_2 can be greatly improved by substituting Mn with other elements having smaller ionic radii ratio, such as Mg and Li.[38, 46, 52, 55] For example, P2-type $Na_{2/3}Mg_{1/3}Mn_{2/3}O_2$ (NMMO) demonstrates a high lattice oxygen redox reversibility of 79% during the initial cycle with the capacity retention of 87% after 100 cycles, which could be related to the strong ionic bonding of Mg with O.[38, 55] Here we attribute the poor oxygen redox reversibility of NaNMO to the weak ionic bonding nature of Ni-O compared with that of Mg-O for NMMO, which cannot inhibit the irreversible transformation of oxidized species to oxygen gas.[55]

Surprisingly, the formation and decomposition of CO_3^{2-} species is reversible, as observed both on the surface (Figure S3b) and in the bulk (Figure 6 and S4b), although the intensity of formed CO_3^{2-} is gradually decreased with cycling. A detailed understanding of such behavior of CO_3^{2-} species is complicated and several points are worth mentioning: (1) although the change of the CO_3^{2-} content is more apparent at the surface (Figure S3b), it is also detectable in the bulk (Figure S4b and 6). It is possible that a reaction takes place between discharged NaNMO and the electrolyte, resulting in the formation of CO_3^{2-} on the surface and in the bulk.[56] (2) The breathing behavior of CO_3^{2-} species on the surface indicates the instability of formed cathode-electrolyte interfacial layer, which may be detrimental for the electrochemical performance of NaNMO. (3) The reversible formation of CO_3^{2-} could also contribute to the delivered capacity of NaNMO. (4) The possibility of CO_3^{2-} contamination of the NaNMO electrodes used in this study is pretty low because the sample preparation and measurement processes were well-controlled under zero air exposure conditions. Overall, our preliminary results on the reversible formation of CO_3^{2-} species for NaNMO electrodes described here provide valuable information for understanding the electrode-electrolyte interaction of transition metal oxide electrodes for NIBs.

Conclusions

To summarize, we have comprehensively elucidated the charge compensation and capacity fading mechanism of NaNMO nanoflakes qualitatively and quantitatively by a combination of synchrotron-based sXAS and mRIXS from an atomic level. We show that the bulk Mn^{3+}/Mn^{4+} redox emerges from the first discharge process and is still active upon cycling, although the reversibility is continuously deceasing. We also find that the bulk Ni redox mainly originates from the Ni^{2+}/Ni^{3+} couple, in contrast to the conventional wisdom of the Ni^{2+}/Ni^{4+} couple. The gradual deactivation of the Ni^{2+}/Ni^{3+} redox after 30 cycles may be partially responsible for the capacity fading of NaNMO. The quantitative analysis of Mn and Ni redox provides direct evidence for the continuously reduced average valence state of Mn and Ni upon cycling, leading to the voltage fading. It is also found that the oxygen anions are also involved in the charge compensation process upon charge, mainly in a manner of irreversible oxygen release. In addition, the reversible formation of CO_3^{2-} species for NaNMO both on the surface and in the bulk implies that some additional charge storage reaction may take place between discharged NaNMO and electrolyte.

More importantly, the methodology for quantifying the Mn redox in bulk electrodes through the non-distorted Mn L-edge mRIXS-iPFY can also be extended to other Mn-based oxide cathodes for NIBs, which will play a vital role for the rational design of high-performance TM oxide cathode materials and also push the practical application of NIBs in the near future.

Supporting information

The supporting information is available free of charge in the online version.

Acknowledgements

This work is supported by Collaborative Innovation Center of Suzhou Nano Science & Technology, the Priority Academic Program Development of Jiangsu Higher Education Institutions (PAPD), the 111 Project. The work at Advanced Light Source of the Lawrence Berkeley National Laboratory is supported by the Director, Office of Science, Office of Basic Energy Sciences, of the U.S. Department of Energy under Contract No. DE-AC02-05CH11231.

References

(1) Xu, K. Electrolytes and Interphases in Li-Ion Batteries and Beyond. *Chem. Rev.* **2014,** *114*, 11503-618.

(2) Armand, M.; Tarascon, J.-M. Building Better Batteries. *Nature* **2008,** *451*, 652-657.

(3) Li, M.; Lu, J.; Chen, Z.; Amine, K. 30 Years of Lithium-Ion Batteries. *Adv. Mater.* **2018,** *30*, 1800561.

(4) Chu, S.; Cui, Y.; Liu, N. The Path towards Sustainable Energy. *Nature Mater.* **2016,** *16*, 16-22.

(5) Meng, J.; Guo, H.; Niu, C.; Zhao, Y.; Xu, L.; Li, Q.; Mai, L. Advances in Structure and Property Optimizations of Battery Electrode Materials. *Joule* **2017,** *1*, 522.

(6) Lin, D.; Liu, Y.; Cui, Y. Reviving the Lithium Metal Anode for High-Energy Batteries. *Nature*

Nanotech. **2017,** *12*, 194-206.

(7) Nitta, N.; Wu, F.; Lee, J. T.; Yushin, G. Li-ion Battery Materials: Present and Future. *Mater. Today* **2015,** *18*, 252-264.

(8) Zhang, H.; Hasa, I.; Passerini, S. Beyond Insertion for Na-Ion Batteries: Nanostructured Alloying and Conversion Anode Materials. *Adv. Energy Mater.* **2018,** *8*, 1702582.

(9) Zheng, X.; Bommier, C.; Luo, W.; Jiang, L.; Hao, Y.; Huang, Y. Sodium Metal Anodes for Room-Temperature Sodium-Ion Batteries: Applications, Challenges and Solutions. *Energy Storage Mater.* **2019,** *16*, 6-23.

(10) Song, J.; Xiao, B.; Lin, Y.; Xu, K.; Li, X. Interphases in Sodium-Ion Batteries. *Adv. Energy Mater.* **2018,** *8*, 1703082.

(11) Yu, L.; Wang, L. P.; Liao, H.; Wang, J.; Feng, Z.; Lev, O.; Loo, J. S. C.; Sougrati, M. T.; Xu, Z. J. Understanding Fundamentals and Reaction Mechanisms of Electrode Materials for Na-Ion Batteries. *Small* **2018,** *14*, e1703338.

(12) Xiao, Y.; Lee, S. H.; Sun, Y.-K. The Application of Metal Sulfides in Sodium Ion Batteries. *Adv. Energy Mater.* **2017,** *7*, 1601329.

(13) Sun, Y.; Guo, S.; Zhou, H. Exploration of Advanced Electrode Materials for Rechargeable Sodium-Ion Batteries. *Adv. Energy Mater.* **2018**, 1800212.

(14) Han, M.; Gonzalo, E.; Singh, G.; Rojo, T. A Comprehensive Review of Sodium Layered Oxides: Powerful Cathodes for Na-Ion Batteries. *Energy Environ. Sci.* **2015,** *8*, 81.

(15) He, K.; Lin, F.; Zhu, Y.; Yu, X.; Li, J.; Lin, R.; Nordlund, D.; Weng, T. C.; Richards, R. M.; Yang, X. Q.; Doeff, M. M.; Stach, E. A.; Mo, Y.; Xin, H. L.; Su, D. Sodiation Kinetics of Metal Oxide Conversion Electrodes: A Comparative Study with Lithiation. *Nano Lett.* **2015,** *15*,

5755-63.

(16) Wang, P.-F.; You, Y.; Yin, Y.-X.; Guo, Y.-G. Layered Oxide Cathodes for Sodium-Ion Batteries: Phase Transition, Air Stability, and Performance. *Adv. Energy Mater.* **2018,** *8*, 1701912.

(17) Jiang, K.; Zhang, X.; Li, H.; Zhang, X.; He, P.; Guo, S.; Zhou, H. Suppressed the High-Voltage Phase Transition of P2-Type Oxide Cathode for High-Performance Sodium-Ion Batteries. *ACS Appl. Mater. Interfaces* **2019,** *11*, 14848-14853.

(18) Wang, P.-F.; Yao, H.-R.; Liu, X.-Y.; Yin, Y.-X.; Zhang, J.-N.; Wen, Y.; Yu, X.; Gu, L.; Guo, Y.-G. Na+/Vacancy Disordering Promises High-Rate Na-Ion Batteries. *Science Adv.* **2018,** *4*, eaar6018.

(19) Wang, Y.; Yu, X.; Xu, S.; Bai, J.; Xiao, R.; Hu, Y. S.; Li, H.; Yang, X. Q.; Chen, L.; Huang, X. A Zero-Strain Layered Metal Oxide as the Negative Electrode for Long-Life Sodium-Ion Batteries. *Nature Commun.* **2013,** *4*, 2365.

(20) Clément, R. J.; Bruce, P. G.; Grey, C. P. Review—Manganese-Based P2-Type Transition Metal Oxides as Sodium-Ion Battery Cathode Materials. *J. Electrochem. Soc.* **2015,** *162*, A2589-A2604.

(21) Dai, K.; Mao, J.; Song, X.; Battaglia, V.; Liu, G. J. J. o. P. S. $Na_{0.44}MnO_2$ with very Fast Sodium Diffusion and Stable Cycling Synthesized via Polyvinylpyrrolidone-Combustion Method. *Nano Energy* **2015,** *285*, 161-168.

(22) Caballero, A.; Hernan, L.; Morales, J.; Sanchez, L.; Pena, J. S.; Aranda, M. J. J. o. M. C. Synthesis and Characterization of High-Temperature Hexagonal P2-$Na_{0.6}MnO_2$ and Its Electrochemical Behaviour as Cathode in Sodium Cells. *J. Mater. Chem.* **2002,** *12*, 1142-1147.

(23) Duffort, V.; Talaie, E.; Black, R.; Nazar, L. F. Uptake of CO_2 in Layered

P2-$Na_{0.67}Mn_{0.5}Fe_{0.5}O_2$: Insertion of Carbonate Anions. *Chem. Mater.* **2015,** *27*, 2515-2524.

(24) Wang, H.; Yang, B.; Liao, X.-Z.; Xu, J.; Yang, D.; He, Y.-S.; Ma, Z.-F. Electrochemical Properties of P2-$Na_{2/3}[Ni_{1/3}Mn_{2/3}]O_2$ Cathode Material for Sodium Ion Batteries when Cycled in Different Voltage Ranges. *Electrochimica Acta* **2013,** *113*, 200-204.

(25) Lu, Z.; Dahn, J. In Situ X-Ray Diffraction Study of P2 $Na_{2/3}[Ni_{1/3}Mn_{2/3}]O_2$. *J. Electrochem. Soc.* **2001,** *148*, A1225-A1229.

(26) Lee, S. Y.; Kim, J. H.; Kang, Y. C. Electrochemical Properties of P2-type $Na_{2/3}Ni_{1/3}Mn_{2/3}O_2$ Plates Synthesized by Spray Pyrolysis Process for Sodium-Ion Batteries. *Electrochimica Acta* **2017,** *225*, 86-92.

(27) Risthaus, T.; Zhou, D.; Cao, X.; He, X.; Qiu, B.; Wang, J.; Zhang, L.; Liu, Z.; Paillard, E.; Schumacher, G.; Winter, M.; Li, J. A High-Capacity P2 $Na_{2/3}Ni_{1/3}Mn_{2/3}O_2$ Cathode Material for Sodium Ion Batteries with Oxygen Activity. *J. Power Sources* **2018,** *395*, 16-24.

(28) Yoda, Y.; Kubota, K.; Isozumi, H.; Horiba, T.; Komaba, S. Poly-gamma-glutamate Binder To Enhance Electrode Performances of P2-$Na_{2/3}Ni_{1/3}Mn_{2/3}O_2$ for Na-Ion Batteries. *ACS Appl. Mater. Interfaces* **2018,** *10*, 10986-10997.

(29) Zheng, X.; Li, P.; Zhu, H.; Rui, K.; Zhao, G.; Shu, J.; Xu, X.; Sun, W.; Dou, S. X. New Insights into Understanding the Exceptional Electrochemical Performance of P2-type Manganese-based Layered Oxide Cathode for Sodium Ion Batteries. *Energy Storage Mater.* **2018,** *15*, 257-265.

(30) Wen, Y.; Wang, B.; Zeng, G.; Nogita, K.; Ye, D.; Wang, L. Electrochemical and Structural Study of Layered P2-type $Na_{(2/3)}Ni_{(1/3)}Mn_{(2/3)}O_2$ as Cathode Material for Sodium-Ion Battery. *Chem. Asian J.* **2015,** *10*, 661-6.

(31) Alvarado, J.; Ma, C.; Wang, S.; Nguyen, K.; Kodur, M.; Meng, Y. S. Improvement of the Cathode Electrolyte Interphase on P2-$Na_{2/3}Ni_{1/3}Mn_{2/3}O_2$ by Atomic Layer Deposition. *ACS Appl. Mater. Interfaces* **2017,** *9*, 26518-26530.

(32) Ma, C.; Alvarado, J.; Xu, J.; Clement, R. J.; Kodur, M.; Tong, W.; Grey, C. P.; Meng, Y. S. Exploring Oxygen Activity in the High Energy P2-Type $Na_{0.78}Ni_{0.23}Mn_{0.69}O_2$ Cathode Material for Na-Ion Batteries. *J. Am. Chem. Soc.* **2017,** *139*, 4835-4845.

(33) Wu, X.; Xu, G. L.; Zhong, G.; Gong, Z.; McDonald, M. J.; Zheng, S.; Fu, R.; Chen, Z.; Amine, K.; Yang, Y. Insights into the Effects of Zinc Doping on Structural Phase Transition of P2-Type Sodium Nickel Manganese Oxide Cathodes for High-Energy Sodium Ion Batteries. *ACS Appl. Mater. Interfaces* **2016,** *8*, 22227-37.

(34) Yang, Q.; Wang, P. F.; Guo, J. Z.; Chen, Z. M.; Pang, W. L.; Huang, K. C.; Guo, Y. G.; Wu, X. L.; Zhang, J. P. Advanced P2-$Na_{2/3}Ni_{1/3}Mn_{7/12}Fe_{1/12}O_2$ Cathode Material with Suppressed P2-O2 Phase Transition toward High-Performance Sodium-Ion Battery. *ACS Appl. Mater. Interfaces* **2018,** *10*, 34272-34282.

(35) Wang, P. F.; You, Y.; Yin, Y. X.; Wang, Y. S.; Wan, L. J.; Gu, L.; Guo, Y. G. Suppressing the P2–O2 Phase Transition of $Na_{0.67}Mn_{0.67}Ni_{0.33}O_2$ by Magnesium Substitution for Improved Sodium-Ion Batteries. *Angew. Chem. Int Ed.* **2016,** *55*, 7445-7449.

(36) Lee, D. H.; Xu, J.; Meng, Y. S. An Advanced Cathode for Na-Ion Batteries with High Rate and Excellent Structural Stability. *Phys. Chem. Chem. Phys.* **2013,** *15*, 3304-12.

(37) Liu, Y.; Fang, X.; Zhang, A.; Shen, C.; Liu, Q.; Enaya, H. A.; Zhou, C. Layered P2-$Na_{2/3}[Ni_{1/3}Mn_{2/3}]O_2$ as High-Voltage Cathode for Sodium-Ion Batteries: The Capacity Decay Mechanism and Al_2O_3 Surface Modification. *Nano Energy* **2016,** *27*, 27-34.

(38) Dai, K.; Wu, J.; Zhuo, Z.; Li, Q.; Sallis, S.; Mao, J.; Ai, G.; Sun, C.; Li, Z.; Gent, W. E.; Chueh, W. C.; Chuang, Y.-d.; Zeng, R.; Shen, Z.-x.; Pan, F.; Yan, S.; Piper, L. F. J.; Hussain, Z.; Liu, G.; Yang, W. High Reversibility of Lattice Oxygen Redox Quantified by Direct Bulk Probes of Both Anionic and Cationic Redox Reactions. *Joule* **2018,** *3*, 1-24.

(39) Wu, J.; Song, J.; Dai, K.; Zhuo, Z.; Wray, L. A.; Liu, G.; Shen, Z. X.; Zeng, R.; Lu, Y.; Yang, W. Modification of Transition-Metal Redox by Interstitial Water in Hexacyanometallate Electrodes for Sodium-Ion Batteries. *J. Am. Chem. Soc.* **2017,** *139*, 18358.

(40) Li, Q.; Qiao, R.; Wray, L. A.; Chen, J.; Zhuo, Z.; Chen, Y.; Yan, S.; Pan, F.; Hussain, Z.; Yang, W. Quantitative Probe of the Transition Metal Redox in Battery Electrodes through Soft X-ray Absorption Spectroscopy. *J Phys. D: Appl. Phys.* **2016,** *49*, 413003.

(41) Lin, F.; Liu, Y.; Yu, X.; Cheng, L.; Singer, A.; Shpyrko, O. G.; Xin, H. L.; Tamura, N.; Tian, C.; Weng, T. C.; Yang, X. Q.; Meng, Y. S.; Nordlund, D.; Yang, W.; Doeff, M. M. Synchrotron X-ray Analytical Techniques for Studying Materials Electrochemistry in Rechargeable Batteries. *Chem. Rev.* **2017,** *117*, 13123.

(42) Achkar, A. J.; Regier, T. Z.; Wadati, H.; Kim, Y. J.; Zhang, H.; Hawthorn, D. G. Bulk Sensitive X-ray Absorption Spectroscopy Free of Self-Absorption Effects. *Phys. Rev. B* **2011,** *83*, 081106.

(43) Qiao, R.; Dai, K.; Mao, J.; Weng, T.-C.; Sokaras, D.; Nordlund, D.; Song, X.; Battaglia, V. S.; Hussain, Z.; Liu, G.; Yang, W. Revealing and Suppressing Surface Mn(II) Formation of $Na_{0.44}MnO_2$ Electrodes for Na-Ion Batteries. *Nano Energy* **2015,** *16*, 186-195.

(44) Xu, J.; Sun, M.; Qiao, R.; Renfrew, S. E.; Ma, L.; Wu, T.; Hwang, S.; Nordlund, D.; Su, D.; Amine, K.; Lu, J.; McCloskey, B. D.; Yang, W.; Tong, W. Elucidating Anionic Oxygen Activity in

Lithium-rich Layered Oxides. *Nature Commun.* **2018,** *9*, 947.

(45) Gent, W. E.; Lim, K.; Liang, Y.; Li, Q.; Barnes, T.; Ahn, S. J.; Stone, K. H.; McIntire, M.; Hong, J.; Song, J. H.; Li, Y.; Mehta, A.; Ermon, S.; Tyliszczak, T.; Kilcoyne, D.; Vine, D.; Park, J. H.; Doo, S. K.; Toney, M. F.; Yang, W.; Prendergast, D.; Chueh, W. C. Coupling between Oxygen Redox and Cation Migration Explains Unusual Electrochemistry in Lithium-rich Layered Oxides. *Nature Commun.* **2017,** *8*, 2091.

(46) Yabuuchi, N.; Hara, R.; Kubota, K.; Paulsen, J.; Kumakura, S.; Komaba, S. A new Electrode Material for Rechargeable Sodium Batteries: P2-type $Na_{2/3}[Mg_{0.28}Mn_{0.72}]O_2$ with Anomalously High Reversible Capacity. *J. Mater. Chem. A* **2014,** *2*, 16851-16855.

(47) Wu, J.; Sallis, S.; Qiao, R.; Li, Q.; Zhuo, Z.; Dai, K.; Guo, Z.; Yang, W. Elemental-sensitive Detection of the Chemistry in Batteries through Soft X-ray Absorption Spectroscopy and Resonant Inelastic X-ray Scattering. *Journal of Visualized Experiments* **2018,** e57415.

(48) Qiao, R.; Wang, Y.; Olalde-Velasco, P.; Li, H.; Hu, Y.-S.; Yang, W. Direct Evidence of Gradient Mn(II) Evolution at Charged States in $LiNi_{0.5}Mn_{1.5}O_4$ Electrodes with Capacity Fading. *J. Power Sources* **2015,** *273*, 1120-1126.

(49) Wu, J.; Li, Q.; Sallis, S.; Zhuo, Z.; Gent, E. W.; Chueh, C. W.; Yan, S.; Chuang, Y.-d.; Yang, W. Fingerprint Oxygen Redox Reactions in Batteries through High-Efficiency Mapping of Resonant Inelastic X-ray Scattering. *Condensed Matter.* **2019,** *4*.

(50) Yang, W.; Devereaux, T. P. Anionic and Cationic Redox and Interfaces in Batteries: Advances from Soft X-ray Absorption Spectroscopy to Resonant Inelastic Scattering. *J. Power Sources* **2018,** *389*, 188-197.

(51) Luo, K.; Roberts, M. R.; Hao, R.; Guerrini, N.; Pickup, D. M.; Liu, Y. S.; Edstrom, K.; Guo,

J.; Chadwick, A. V.; Duda, L. C.; Bruce, P. G. Charge-Compensation in 3d-Transition-Metal-Oxide Intercalation Cathodes through the Generation of Localized Electron Holes on Oxygen. *Nature Chem.* **2016,** *8*, 684-91.

(52) Rong, X.; Liu, J.; Hu, E.; Liu, Y.; Wang, Y.; Wu, J.; Yu, X.; Page, K.; Hu, Y.-S.; Yang, W.; Li, H.; Yang, X.-Q.; Chen, L.; Huang, X. Structure-Induced Reversible Anionic Redox Activity in Na Layered Oxide Cathode. *Joule* **2018,** *2*, 125-140.

(53) Mortemard de Boisse, B.; Liu, G.; Ma, J.; Nishimura, S.; Chung, S. C.; Kiuchi, H.; Harada, Y.; Kikkawa, J.; Kobayashi, Y.; Okubo, M.; Yamada, A. Intermediate Honeycomb Ordering to Trigger Oxygen Redox Chemistry in Layered Battery Electrode. *Nature Commun.* **2016,** *7*, 11397.

(54) Hu, E.; Yu, X.; Lin, R.; Bi, X.; Lu, J.; Bak, S.; Nam, K.-W.; Xin, H. L.; Jaye, C.; Fischer, D. A.; Amine, K.; Yang, X.-Q. Evolution of Redox Couples in Li- and Mn-rich Cathode Materials and Mitigation of Voltage Fade by Reducing Oxygen Release. *Nature Energy* **2018，** *3*， 690-698.

(55) Song, B.; Hu, E.; Liu, J.; Zhang, Y.; Yang, X.-Q.; Nanda, J.; Huq, A.; Page, K. A Novel P3-type $Na_{2/3}Mg_{1/3}Mn_{2/3}O_2$ as High Capacity Sodium-Ion Cathode Using Reversible Oxygen Redox. *J. Mater. Chem. A* **2019,** *7*, 1491-1498.

(56)Bak, S.-M.; Qiao, R.; Yang, W.; Lee, S.; Yu, X.; Anasori, B.; Lee, H.; Gogotsi, Y.; Yang, X.-Q. Na-Ion Intercalation and Charge Storage Mechanism in 2D Vanadium Carbide. *Adv. Energy Mater.* **2017,** *7*, 1700959.